cience and Engineering Center
University of Wisconsin-Madison

A Report to

National Earth Satellite Service
National Oceanic and Atmospheric Administration

# A REPORT from the

# Cooperative Institute for Meteorological Satellite Studies

A Report to

National Earth Satellite Service
National Oceanic and Atmospheric Administration

for

# A Demonstration of a Satellite Microwave Technique for the Measurement of Rainfall in Agricultural Areas

Contract #NA-80-SAC-00742
University of Wisconsin Account #144-P961

for the period of

1 May 1983 to 1 May 1984

submitted by

Roy W. Spencer
David W. Martin

Space Science and Engineering Center
at the University of Wisconsin-Madison
1225 West Dayton Street
Madison, Wisconsin 53706
(608) 262-0544

May, 1984

Table of Contents

Abstract

Rain rate algorithms for spring, summer, and fall are described which have been developed from comparisons between the brightness temperatures measured by the Nimbus-7 Scanning Multichannel Microwave Radiometer (SMMR) and rain rates derived from operational WSR-57 radars over land. Data were utilized from a total of twenty-five SMMR passes and 234 radars, resulting in ~12000 observations of ~1600 $km^2$ areas. Multiple correlation coefficients of 0.63, 0.80, and 0.75 are achieved for the spring, summer, and fall algorithms, respectively. Most of this information is in the form of multispectral contrast in brightness temperature, which is interpreted as a measurement of the degree to which the land emitted radiation is attenuated by the rain systems. The SMMR 37 GHz channel has more information on rain rate than any other channel. The land emitted radiation is implicitly measured by the lower frequency channels of the SMMR. This land radiation measurement is important because synoptic and seasonal variations in land thermometric temperatures result in brightness temperature variations which might be confused with those variations due to rain, and thus must be considered in any generalized passive microwave rain estimation algorithm. Polarization screening at 37 GHz is found to be sufficient to screen out cases of wet ground, which is only important when the ground is relatively vegetation free. Heavy rain cases are found to be a significant part of the algorithms' success, because of the strong microwave signature (low brightness temperatures) that result from the presence of precipitation sized ice in the upper portions of heavily precipitating storms. If IR data are combined with the summer microwave data, an improved (0.85) correlation is achieved. Based upon past and present work on visible and IR rain estimation at the University of

Wisconsin, a procedure for the synthesis of microwave, visible, and IR data into a rain estimation scheme is outlined.

Acknowledgements

We are very grateful for the assistance provided during the course of this work by Drs. Barry Hinton, Norman Grody, James Weinman, William Olson and Mr. Michael Howland. David Santek was instrumental in developing the computer programs for the display and manipulation of SMMR data on McIDAS. SMMR data were supplied by Dr. Per Gloersen and Mr. William Abbott. Angela Crowell typed the manuscript.

## 1. INTRODUCTION

The remote sensing of rainfall from satellites has, most commonly, been attempted with visible and infrared (IR) observations. These techniques rely on the existence of some relationship between the occurrence or intensity of rainfall within a cloud and the appearance or behavior of the cloud top as observed by the satellite (Barrett and Martin, 1981). Microwave radiation at window frequencies below 40 GHz easily penetrates clouds but not precipitation. To estimate rain rates with satellite passive microwave observations at these frequencies, the rain must have a significantly different electromagnetic signature from its surroundings, whether land or ocean. This condition is easily met over the ocean because the ocean has a relatively uniform and low brightness temperature ($T_B = \varepsilon T$) due to its low emissivity ($\varepsilon \sim 0.5$), while the rain has a mostly uniform and high emissivity ($\varepsilon \sim 0.9$) and thus, a high brightness temperature. Thus, theoretical and empirical treatments of the problem have, with some differences, indicated that rain rates over the ocean are retrievable (Wilheit et al., 1977; Huang and Liou, 1983; Spencer et al., 1983a). Land, however, has an emissivity that is much closer to that of rain and is more variable, due to variations in soil moisture and roughness. This results in some ambiguity between wet land surfaces and rain (e.g. Rodgers and Siddalingaiah, 1983). Even if the background were uniform, theoretical results suggested that only light rain rates would be detectable (Savage and Weinman, 1975; Weinman and Guetter, 1977).

More recently, Spencer et al. (1983b) documented the existence of very low 37 GHz brightness temperatures from the Nimbus-7 SMMR (Scanning Multichannel Microwave Radiometer) in conjunction with heavy thunderstorm rainfalls over land. The SMMR is a ten channel, five frequency instrument

that scans conically and thus maintains a nearly constant viewing angle of 50° at the surface of the earth (Table 1). The low brightness temperatures were attributed to the presence of precipitation-size ice particles in the upper portions of the storms. This work led to the development of a multifrequency rain estimation algorithm based upon comparisons of rain rates from operational WSR-57 radars and the microwave observations of the SMMR over the United States (U.S.) during the summer (Spencer et al., 1983c).

The purpose here is to describe the development of spring and fall rain rate algorithms, to investigate the forms of the spring, summer, and fall algorithms, and to compare the microwave with infrared data in terms of rain rate information content.

## 2. METHOD

### 2.1 Radar - Microwave - IR Comparisons

Radar rain rates from operational WSR-57 radars were compared to SMMR brightness temperatures to determine how much information on rain rate is contained in the SMMR observations. This was done for eight SMMR passes during the fall of 1978 and the spring of 1979, and nine SMMR passes during the summer of 1979. These dates and times are listed in Table 2, along with the number of radars involved in the comparisons. The region of interest was east of the Rocky Mountains and west of the Appalachian Mountains of the U.S., an area primarily comprised of croplands, woodlands, and pasture. The analysis days were chosen by comparing the locations of SMMR swaths to radar summary charts produced hourly by the National Meteorological Center. Because the fraction of the SMMR pass covered by rain was typically small, only those cases having the most widespread rains

| | Frequency (GHz) | | | | |
|---|---|---|---|---|---|
| | 37 | 21 | 18 | 10.7 | 6.6 |
| Polarization | V,H | V,H | V,H | V,H | V,H |
| wavelength (cm) | 0.81 | 1.36 | 1.66 | 2.80 | 4.54 |
| field of view (km) | 22 | 37 | 43 | 74 | 120 |

Table 1 SMMR frequencies and integrated field of view sizes at the earth's surface. Integrated fields of view are approximately square in shape. Horizontal (H) and vertical (V) polarizations are sampled at each frequency. This is accomplished with two radiometers at 37 GHz, and one radiometer at each of the lower frequencies, which is shared between H and V on alternating scans of the instrument. In this paper the channels and their brightness temperatures will be referred to by a combination of the frequency and polarization, e.g. H37 refers to the horizontally polarized 37 GHz brightness temperature. Further information on the Nimbus-7 SMMR instrument is contained in Gloersen and Hardis (1978).

| Spring, 1979 | | | Summer, 1979 | | | Fall, 1978 | | |
|---|---|---|---|---|---|---|---|---|
| Date/time | # radars | # records | Date/time | # radars | # records | Date/time | # radars | # records |
| 19 March 0630 | 14 | 667 | 4 May 0645 | 4 | 236 | 6 November 0640 | 9 | 433 |
| 29 March 1745 | 12 | 585 | 19 June 1715 | 7 | 321 | 15 November 1730 | 8 | 466 |
| 31 March 0640 | 15 | 762 | 21 June 0610 | 8 | 473 | 17 November 0625 | 8 | 357 |
| 2 April 1710 | 12 | 606 | 1 July 1720 | 14 | 770 | 27 November 0555 | 8 | 362 |
| 4 April 0610 | 11 | 607 | 3 July 1800 | 10 | 550 | 3 December 0555 | 7 | 41 |
| 18 April 0700 | 8 | 390 | 5 July 0700 | 9 | 354 | 3 December 1735 | 7 | 317 |
| 20 April 1735 | 14 | 696 | 5 July 1700 | 7 | 497 | 7 December 1700 | 5 | 355 |
| 26 April 0600 | 7 | 440 | 7 July 1730 | 17 | 879 | 9 December 0600 | 4 | 284 |
| | | | 9 July 0635 | 9 | 590 | | | |

Table 2 Dates and approximate times (GMT) of SMMR and radar coverages included in the analysis for spring, summer, and fall seasons, and the number of 1600 $km^2$ records (containing average SMMR $T_B$'s and radar rain rates) sampled from the data for each date.

where chosen for analysis. Radar microfilm records were inspected for photographic quality, low elevation angles of the radar beam (generally less than 1°), presence of discernible D-VIP (digital video integrator and processor) levels, and viewing times no more than 8 min. different from the SMMR observation times. Those pictures deemed acceptable were registered on a 20 km grid and manually digitized. Each 20 km bin was assigned an average rain rate

$$R = \sum_{1=1}^{N} a_i r_i \qquad (1)$$

where i denotes the VIP level, $a_i$ the area of the bin covered by the i'th VIP level, and $r_i$ the average rain rate represented by that VIP level. The six reflectivity levels displayed by the WSR-57 were assigned average rain rates of 4, 17, 42, 85, 147, and 190 mm $h^{-1}$ (NOAA, 1979). The resulting rain rates are expected to have standard errors of about 60%.

These gridded, averaged rain rates, and corresponding SMMR $T_B$'s were converted into images on the University of Wisconsin's Man-computer Interactive Data Access System (McIDAS; Suomi et al., 1983). All images were remapped to a GOES-east projection to facilitate comparisons with GOES IR data, which were analyzed for the summer dates in Table 2. Locations in SMMR images were checked and corrected (if needed) by comparing the land-water $T_B$ differences to known coastal features. When land is viewed, the corrected locations are probably accurate to within 10 km. However, because of the SMMR viewing angle of 50°, parallax errors of ~10 km are possible in the observations of heavy thunderstorms. Errors from the radar digitization might also approach 10 km. Because of these errors, it was decided that image data sampling on a 20 km grid might introduce an

unacceptable amount of noise, so a rather arbitrary value of 40 km was chosen for the sampling of these images. A 40 km square cursor was moved across the images, and average radar rain rates, IR temperatures, and SMMR $T_B$'s were computed. Data from each cursor position will hereafter be referred to as a 'record'. These records were then statistically analyzed with a stepwise, least squares, multiple linear regression procedure (Dixon, 1983).

### 2.2 Rain Gage - Microwave Comparisons

For the summer dates listed in Table 2, hourly rain gage totals were also compared to the SMMR brightness temperatures. Those U.S. cooperative network gages that fell within the SMMR coverage area were sampled at the first hours following the SMMR observation times. A 40 km cursor box was centered on each gage location in the SMMR images, and average SMMR $T_B$'s were computed within that box. Subsequent statistical analyses were carried out as described in the previous section.

## 3. RAIN SYSTEM SUMMARY

Interpretation of the results of the SMMR and radar comparisons is facilitated by a knowledge of the characteristics of the rain systems contained in the data sets. A review of the synoptic situations on each day revealed that the summer rain storms were almost always convective. The spring and fall systems were more widespread and uniform (stratiform). Fig. 1 shows composited radar images of all the rain systems in the spring, summer, and fall data sets. The most intense storms occurred during the summer, which is quantitatively revealed in Fig. 2, a comparison of the frequency distribution of rain rates between the spring, summer, and fall seasons. It must be remembered that these rates have been averaged over

1600 $km^2$ areas, and thus are in many cases considerably smaller than the peak rates found within the systems.

## 4. THE 21 JUNE 1979 CASE

To illustrate the effect of rain on the different SMMR channels, Fig. 3 shows radar and vertically polarized 37, 18, and 10.7 GHz images (V37, V18, V10.7) from 0610 GMT 21 June 1979. It is obvious that, of the three SMMR images, the 37 GHz image (Fig. 3b) is the best representation of the radar image (Fig. 3a) This is revealed as a negative visual correlation between rain rate and $T_B$, both of which vary in direct proportion to image brightness.

It can be seen from Fig. 3c and 3d that the 18 and 10.7 channels are much less affected by the rain than the 37 GHz channel is. This is because rain becomes increasingly transparent and the SMMR footprint size increases as the frequency decreases. The effect of soil and vegetation on the sensed radiation then becomes greater. Kirdiashev et al. (1979), Jackson et al. (1982), and Mo et al. (1982) have shown that the penetration of vegetation by microwave radiation is directly related to the moisture content of the vegetation canopy. A thick canopy of soybeans or corn, for instance, will be virtually opaque to the transfer of radiation from 37 to 6.6 GHz. Wheat, on the other hand, will be somewhat transparent at 6.6 GHz because of the sparseness and low moisture content of the cover, but still will be quite opaque at 37 GHz. Thus, we might expect that the form of any multifrequency rain estimation algorithm should depend somewhat on the character of the vegetation.

## 5. RESULTS

### 5.1 Radar-Microwave Comparisons

#### 5.1.1 data screening

Initially data were screened to remove those observations of 1) oceans, lakes, or wet soil surfaces, and 2) land surfaces having higher $T_B$'s than any rain cell in the data sample. As noted by Weinman and Guetter (1977) wet soil and water bodies can be distinguished from rain by their large values of 37 GHz polarization[1]. They suggested correcting the brightness temperatures by an amount proportional to the polarization value. This was tried with the current data set, but a simple screening procedure was found to be slightly more effective. The screening was based upon measurements from the data sets in Table 2 indicating that 37 GHz observations of rainclouds on a 40 km scale almost never have polarizations exceeding 15°C over land.

Individual SMMR 37 GHz observations (20 km resolution) reveal that the cores of intense storms have even larger polarizations, exceeding 20° when H37 falls below 175 K. This increase in polarization with increasing storm intensity is probably related to the shape and orientation of ice particles in the upper portions of storms.

The 37 GHz observations of water and wet soil were found to have polarizations far exceeding 16°C, with increasing polarization indicating increasing moisture content and/or reduced vegetative cover. These results are in contrast to the results of Rodgers and Siddalingaiah (1983) who found that the average 37 GHz polarization of rain areas was 22°C, while

---

[1] the term 'polarization' in this report, when not accompanied by a modifier, refers to the difference between the vertically and horizontally polarized brightness temperatures ($T_B^V - T_B^H$) at a single frequency.

that of wet soil was only slightly larger (24°C). Those results, however, came from a much smaller data set involving two SMMR passes while the present analysis utilizes data from twenty-five SMMR passes and 234 radars. Their analysis included data from two regions where surface water is relatively abundant (Louisiana and Florida).

It was also found here that rain never occurred when the H37 $T_B$ exceeded 280 K, so initial screening for temperatures above this limit was performed before regression. An additional screening procedure was used to exclude those records near coastal waters where the low frequency observations, by virtue of their large footprints, were also contaminated by the water bodies. This screening took the form of H10.7>225 K, and was only used for the summer data. During the spring and fall this criterion excluded an unacceptably large number of cases of light rain over wet ground. Thus, for the spring and fall, an alternate screening (H18 230K) was utilized.

5.1.2 stratified rain classes

After screening, the SMMR and radar averaged data (records) were grouped into rain intensity intervals: zero; 1 to 10; 11 to 20; (and in the case of the summer data) 21 to 30, and 30 mm $h^{-1}$. The average values of SMMR $T_B$'s at various frequencies for each of these rate rate intervals are shown in Fig. 4. Fig. 4a shows these relationships for the horizontal polarizations while Fig. 4b shows those for the vertical polarizations. It is apparent from both charts that the brightness temperatures for the first three rain intervals are warmest during the summer. At R = 0, the obvious reason for this is that the warmest land surfaces occur during the summer. This variation in land temperature has important implications. Note that

at 37 GHz, the average $T_B$ for rain-free areas during spring and fall corresponds to a rain rate of approximately 6 mm $h^{-1}$ during the summer. At 21 GHz this increases to 14 mm $h^{-1}$. Thus, seasonal (as well as synoptic) changes in the land-atmosphere thermometric temperatures can adversely affect the rain estimates if they are not taken into account in some way.

Note also that the $T_B$'s drop off most at the lower frequencies during the spring, and least during the summer. This is a result of the seasonal variations in vegetative cover and soil moisture. The spring data set contains the most observations of bare or partially covered soil, the moisture content of which leads to a lower emissivity and thus lower $T_B$'s. Additional evidence of this is shown in Fig. 5, a seasonal plot of the values of polarization for the R = 0 rain class. It can be seen that the spring land observations have the highest values of polarization, due to the flat and moist character of the soil compared to that of the vegetated surfaces of fall, and especially summer. Specific examples of these differences are illustrated in Fig. 6, the effective emissivities of partly flooded soil, moist soil, mature corn fields, forest, and Amazon jungle at 37, 18, and 6.6 GHz. The effective emissivities of all of the vegetated surfaces are essentially the same (to within the accuracy allowed by the estimation of temperatures with GOES-east IR data), while those of the exposed moist partially flooded soil surfaces are lower, especially at the lower frequencies. Thus, well vegetated surfaces provide a radiometrically uniform background. Partly flooded, exposed soils will be screened out by the 37 GHz polarization screening (e.g. the bottom curve on Fig. 6). However, the exposed soils which are too dry to give large 37 GHz polarizations may be troublesome because moisture variations within the soil can produce variable $T_B$'s in the lower frequencies.

As we inspect the SMMR $T_B$'s for the second and third rain classes (1 to 10, 11 to 20 mm $h^{-1}$) in Fig. 4 we note that the summer classes appear to be the most separable from the R = 0 class. The two heaviest rain classes (21 to 30, 30 mm $h^{-1}$) are even more separable from the R = 0 class, especially at 37 GHz. A curious result is that the R = 30 summer curve is actually warmer at 18 and 10.7 GHz than that of the preceding rain class. This may be due to warmer synoptic conditions attending the storms of the heaviest rain class. In stark contrast to this behavior is the bottom spring curve which reveals a marked $T_B$ drop at 10.7 and 6.6 GHz at the heaviest rain class. This is most easily interpreted as a result of wetting of the spring soils during the heavier rainfalls. These wet soils were not screened out at 37 GHz because the heavy rain is opaque at 37 GHz, but not at 10.7 and 6.6 GHz.

5.1.3 regression equations

A stepwise multiple linear regression procedure was utilized to derive equations relating the radar rain rate to a linear combination of SMMR brightness temperatures. The regression equations that resulted from the statistical analysis of SMMR $T_B$'s vs. radar rain rates (after screening) are listed in Table 3, along with their performance in terms of multiple correlation (r) and the explained variance of the radar data ($r^2$). Using these correlation measures, the summer equation has the best performance (r = 0.795), the fall is a close second (r = 0.752), and the spring is a rather distant third (r = 0.625).

One of the most evident characteristics of these equations is the similarity of the signs of the coefficients between seasons. Note that all 37 GHz terms have negative coefficients, all 21 and 18 GHz terms have

| | SMMR channel $T_B$ coefficients | | | | | | | | | | | | |
|---|---|---|---|---|---|---|---|---|---|---|---|---|---|
| | const. | H37 | V37 | H21 | V21 | H18 | V18 | H10.7 | V10.7 | H6.6 | V6.6 | r | $r^2$ |
| spring | 38.3 | -.107 | -.442 | .279 | .119 | .107 | .105 | -.109 | -.121 | X | .034 | .625 | .391 |
| summer | 32.6 | -.408 | -.378 | .215 | .137 | .406 | .090 | -.242 | .062 | * | * | .795 | .631 |
| fall | 49.9 | -.157 | -.789 | .437 | .261 | .055 | .258 | -.136 | -.102 | X | X | .752 | .565 |

* - not included in the analysis X - not chosen by the regression procedure

Table 3 SMMR rain rate regression equations and their performance for spring, summer, and fall. For the summer the data must satisfy the following criteria: (V37 - H37) $\leq 16^{o}$C and H37 < 280K and H10.7 > 225K. For the spring and fall the data must satisfy: (V37 - H37) $\leq 16^{o}$C and H18 > 230K. The total number of records before screening/after screening are: spring (4753/3031); summer (4663/3782); fall (2615/2288).

positive coefficients and five of the six 10.7 GHz terms have negative coefficients. This is an interesting result in light of the fact that all channels for all three seasons were, individually, negatively correlated with radar rain rate. These differing coefficient signs can be explained by synoptic and seasonal variations in thermometric temperatures. The equations show that the rain rate is, to a first approximation, proportional to the difference between the 37 GHz $T_B$'s and the 21 and 18 GHz $T_B$'s. The 37 GHz terms (with negative coefficients) reflect generally lower $T_B$'s for rain cells than for land. The 21 and 18 GHz terms (with the positive coefficients) can be interpreted as providing information on the variability of thermometric temperatures. Implicitly they measure the land contribution in the vicinity of the rain cell, thus reducing the ambiguity of whether variations in $T_B$ are due to rain activity or due to land temperature variations. The rain contribution to the 21 and 18 GHz radiances is still present, but effectively cancels with that which has previously been provided by the 37 GHz channel. The negative coefficients on the 10.7 GHz terms might represent additional rain-attenuated information that is not contained in the 37 GHz measurements. This is quite possible because the upper portions of the rain layer are sampled at 37 GHz while the 10.7 GHz measurements have their contribution from much lower in the rain layer (Weinman and Wu, personal communication). That so many channels are included in the equations is explainable as either reduction of noise in the measurements or by additional physical processes which have not been accounted for and are not immediately apparent.

Fig. 7 illustrates the relative importance of each regression step in reducing the unexplained variance of the rain rates. For the spring, summer, and fall equations it can be seen that the 37 GHz and 21 GHz

channels (the first two regression steps) provide most of the available information on rain rate. It is of considerable interest to know what effect the heavier rain cases in the summer data have on the algorithm performance. If only those records that have $R < 20$ are analyzed, about 4% of the non-zero rain cases are omitted, but the explained variance is reduced 11% (the dotted curve in Fig. 7). Therefore the heavier rain cases are significant contributors to the success of the summer microwave algorithm. The poorer performance of this modified summer equation (restricted to light rain rates) compared to the fall equation is probably a result of radar-derived rain rate accuracy. The fall radar microfilm images had a better overall quality than those of the summer.

As reported by Spencer et al. (1983c), the summer equation was tested on an independent data set (one SMMR pass, 13 radars). The identical correlation with rain rate (0.80) was virtually identical to that found for the dependent data set (0.79). Independent tests of the spring and fall algorithms were not performed because the results of those tests would only approach the significance of the dependent data set analysis if the sample sizes were roughly the same.

### 5.2 Gage-Microwave Comparisons

If one hour rain gage totals, instead of the radar rain rates, are compared to the SMMR data, the correlations are greatly diminished. In Fig. 7 we see that only two steps were completed by the regression, with only 9% of the variance of the gage totals being explainable by the SMMR $T_B$'s. Such a poor result can be partly attributed to the poor correlation

of one hour gage totals with rain rates averaged over a 1600 $km^2$ area. This is supported by a correlation of 0.299 between the radar rain rates and the gage totals. A virtually identical correlation exists between the SMMR gage algorithm and the gage totals (0.294).

### 5.3 Radar-IR Comparisons

The GOES-east IR temperatures were also found to contain significant information on rain rate during the summer. From the 4663 comparisons of radar and IR data (averaged over 1600 $km^2$ areas) it was found that rain never occurred when IR temperature exceeded 280 K. It was also found that the relationship between IR temperature and radar rain rate is highly nonlinear. The rain rates were compared to different powers of (280 K - IR) to find an optimal functional relationship between the two types of data (Fig. 8). Note that 46% of the radar variance can be explained by an twelfth power of (280 K - IR). This compares to 21% of the variance with only a linear comparison to IR d.c. The nonlinearity arises because of the unbalanced situation that significant rains do not often occur in the absence of cold clouds, but cold clouds do often occur in the absence of significant rains. In contrast to this situation, microwave observations of low, unpolarized 37 GHz brightness temperatures will often occur in the presence of significant rains, and heavy rains will almost always be associated with low brightness temperatures. Thus, a strong IR signature (very low temperature) will have a larger ambiguity concerning the location and intensity of rain than will a strong microwave signature (very low $T_B$).

If microwave screening is combined with IR screening (IR 280 K), and then IR terms are entered into the regression procedure along with the SMMR $T_B$'s, an improved rain rate equation results (Table 4). The explained

Table 4 Combined SMMR and GOES-east IR rain rate regression equation for the summer season. Data had to satisfy four requirements: IR d.c. 100; (V37-H37) 16°C; H37 280 K, and H10.7 225 K.

| | regression step number | | | | | | | | |
|---|---|---|---|---|---|---|---|---|---|
| | 0 | 1 | 2 | 3 | 4 | 5 | 6 | 7 | 8 |
| variable | | V37 | V21 | $IR^{18}$ | H21 | H37 | H18 | H10 | V18 |
| coefficient | 35.0 | -.323 | .120 | $1.2 \times 10^{35}$ | .106 | -.337 | .400 | -.189 | .095 |
| r | | .711 | .796 | .832 | .836 | .842 | .845 | .852 | .853 |
| $r^2$ | | .505 | .633 | .692 | .700 | .708 | .714 | .726 | .728 |

radar variance increases from 63% for the microwave-only equation to nearly 73% with IR screening and IR terms. This improvement (10%) is attributable to only a crude treatment of the IR data, and further improvement might be expected with a more detailed treatment.

## 6. SYNTHESIZING MICROWAVE WITH INFRARED

The demonstration that rain information is present in microwave observations raises the question of how microwave and visible/infrared observations can effectively be combined. For the operational estimation of cropland rainfall through the rest of the present decade this is a question of some importance.

Our approach rests on two premises:

1) A small investment in automation will pay off in the long run, and

2) infrared-rainfall relations vary much more than microwave-rainfall relations.

As corollaries of these the following elements of a synthesis are suggested.

1) Screen infrared data by temperature.

2) Apply pattern recognition to (screened) infrared data.

3) Use microwave observations to tune infrared temperature thresholds.

4) Estimate rainfall on a grid (in latitude and longitude).

5) Reserve the meteorologist for oversight and correction.

The McGill University-Canadian Atmospheric Environment Service nowcasts of summertime rain over Ontario and Quebec (Bellon et al., 1980) may be a prototype for this kind of synthesis. During a recent visit to Madison, Dr. Geoff Austin described this forecast system. (Austin heads

the Stormy Weather Group, at McGill, which conceived, designed and built the nowcast system.) Every half hour a 2500 km by 1500 km sector of GOES visible and infrared imagery is "rain calibrated" by means of the McGill weather radar, which is located at the center of the sector. Here "calibration" simply means the selection, by an iterative process, of rain boundaries in the two dimensional domain of infrared temperature and visible brightness, one each for nil, light, moderate and heavy rain rates. By means of these boundaries, pixels through the whole sector are so classified and the satellite visible-infared image becomes a rain map. To give this process a measure of stability, monthly average boundary values serve as first guesses in the selection of the individual boundary values. This system (including nowcasts of rain over the sector) runs unattended in Toronto.

In the rest of this section we will describe several small steps that have been taken toward realizing a synthesis of visible/infrared and microwave data. The section closes with a suggested design for a microwave-infrared rain estimation algorithm.

In December Elen Cutrim completed a dissertation on Amazon rainfall. This project was aimed at estimating monthly rainfall over Amazonia for both wet and dry seasons. That it could be done at all was due to geostationary satellites and the development of geostationary rain algorithms. The contribution of the present grant to the project was support for Martin as an advisor for Ms. Cutrim. The most tangible result of this support was an Amazon calibration for the grid history technique (which is described below).

The title page and abstract of Ms. Cutrim's dissertation are attached as Appendix I. Among the most pertinent findings (for cropland rainfall)

are the following. First, for this deep tropical area the "point" relationship of rainrate and infrared temperature is poor. Second, a fair portion of Amazon rain comes from warm clouds.

Also in December Bonita Lee completed a thesis on pattern recognition. This was intended to answer the question of how much rain information could be extracted from GOES images by means of the spectral and textural measurements which are standard to pattern recognition. The main contributions of the present grant were to underwrite part of Ms. Lee's computer (McIDAS) time and to support Martin as a thesis advisor.

The title page and abstract of Ms. Lee's thesis are attached as Appendix II. (The thesis and a paper submitted for publication in IEEE Transactions are one and the same.) Among the most pertinent findings are the following. First, in the cases studied, most of the rain information was contained in spectral intensity (temperature or brightness). Second, for certain particular types of cloud-rain systems a spectral/textural algorithm can infer rain classes almost as well as a meteorologist and 200 times faster. Third, time change may be an important source of additional information.

One of us (Martin), together with Michael Howland, has been testing a new technique. The technique, called grid history, is aimed at providing estimates of tropical and warm-season mid-latitude daily rainfall by means of visible and infrared geostationary satellite images. Therefore, even though it had a marine inspiration (Martin and Howland, 1982), the technique may have value for estimating rainfall over croplands. The contribution of the present grant to grid history (apart from what has been mentioned above) is to support the writing of a paper describing the method. This paper is to be submitted to Journal of Climate and Applied

Meteorology. A title page and abstract are attached as Appendix III.

Among the more notable findings (in the context of cropland rainfall) are the following. Interactive measurement works. Time change is important; further, over land, rain regime, relief and low level flow must be taken into account. Then estimates of daily rainfall over areas of $10^4$ $km^2$ may be within a factor of two of actual rainfall.

This leads us to a suggestion for a design of a microwave-infrared algorithm. In a pre-processing stage the meteorologist sets the resolution of the analysis grid. This may be small if crops in the region are in a rain-sensitive stage or if the rain is expected to be convective; large, if crops are relatively indifferent to rain or if the rain is expected to be synoptic. In the pre-processing stage, also, coincident microwave and infared data are remapped to a common projection.

The second stage "calibrates" the infared data, in a series of three steps. First, by means of seasonal (and perhaps geographic) regressions, microwave rainfall is estimated. Second, by means of a seasonally and geographically dependent threshold, the extent of rain in the (time and space) matching infrared image is inferred. Third, the threshold is adjusted to achieve a preset level of agreement between microwave and infrared rain areas. Depending on how much information is contained in the imagery these steps might be repeated for moderate and heavy rainrates.

The last stage provides a map of satellite daily rainfall. It proceeds in five steps. First, the adjusted threshold(s) is (are) applied to all infrared images up to the next microwave pass. Second, grid point rainrate is classified as light or heavy by means of temperature, texture and change in temperature from the preceding image. If multiple thresholds have been applied as part of the second stage calibration, grid point

(stage three) rain rates are compared with threshold (stage two) rainrates. Points where rain rates are more than two classes apart are flagged. Third, grid point rain frequencies are summed over that part of the day not covered by microwave observations and converted to (infrared-only) rainfall. Fourth, microwave rainfall is added to infrared rainfall. Fifth and finally, a meteorologist inspects the microwave-infrared map, concentrating on flagged points. By reference to the microwave and infrared images she spots errors and determines corrections. The map is corrected electromechanically, by means of a cursor and keyboard or an electronic tablet.

During daylight hours visible images could also be used. Austin reports satisfactory results, with brightness-normalized images, even at solar zenith angles as large as 80°.

## 7. SUMMARY AND CONCLUSIONS

The passive microwave observations of the Nimbus-7 SMMR have significant and useful information on radar derived rain rates over the United States during the summer and fall. During the spring there is also significant information, but the influence of non-vegetated moist ground on the land background brightness temperatures results in a poor multispectral contrast between light rain systems and their surroundings. A linear combination of most of the SMMR channels (37, 21, 18, 10.7 GHz) provides this information on rain rate. The 37 and 21 GHz channels contain most of the information needed to explain the variance of the radar rain rates, while the 18 and 10.7 GHz provide significant, but smaller improvements.

The rain rate is closely related to the difference between the 37 GHz $T_B$'s and the 21 and 18 GHz $T_B$'s. This difference is interpreted as a

measure of the degree to which the rain attenuates the upwelling land radiation, the land radiation being measured implicitly by the 21 and 18 GHz channels. Synoptic variations in the land thermometric temperatures are thus taken into account, reducing the possibility of misclassifying land as rain when the land is quite cold. Because vegetative cover (and thus the amount of exposed soil) changes seasonally different equations are used to improve performance within seasons. The results are much poorer if rain gauges are used as ground truth. This is probably due to the poor correspondence between 1 hr gage totals and the instantaneous rain rate over a large area. If GOES-east IR data are pooled with the summer microwave data, a 10% increase (to 73%) in the explained variance of the radar rain rates is attained.

It is concluded that passive microwave rain rate estimation over land surfaces is possible, especially when the land background has a relatively constant emissivity. This condition is met most of the time in the middle latitudes during the warm season and in much of the tropics year round, when vegetation covers the surface. Vegetation wetting by dew or rain appears to have little effect on emissivity. The effect of precipitation-sized ice particles is to greatly reduce the 37 GHz $T_B$'s in the presence of heavy rain, and thus improve the rain signal-to-land noise ratio.

References

Barrett, E. C., and D. W. Martin, 1981: The Use of Satellite Data in Rainfall Monitoring. Academic Press, London, 340 pp.

Bellon, A., S. Lovejoy and G. L. Austin, 1980: Combining satellite and radar data for the short-range forecasting of precipitation. Mon. Wea. Rev., 108, 1554-1566.

Dixon, W. J., ed., 1983: BMDP Statistical Software. Berkeley, Univ. of Calif. Press.

Gloersen, P., and L. Hardis, 1978: The Nimbus 7 Users' Guide. National Aeronautics and Space Administration, 213-245.

Huang, R., and K.-N. Liou, 1983: Polarized microwave radiation transfer in precipitating cloudy atmospheres: Applications to window frequencies. J. Geophys. Res., 88, 3885-3893.

Jackson, T. J., T. J. Schmugge, and J. R. Wang, 1982: Passive microwave sensing of soil moisture under vegetation canopies. Water Resources Res., 18, 1137-1142.

Kirdiashev, K. P., A. A. Chukhlantsev, and A. M. Shutko, 1979: Microwave radiation of the Earth's surface in the presence of vegetation cover. Radio Eng. Electron. Phys. Engl. Transl., 24, 256-264.

Lee, B. G., R. T. Chin and D. W. Martin, 1983: Classification of rain cells in satellite imagery. Submitted to IEEE Trans. Geophys. Remote Sensing.

Mo, T., B. J. Choudhury, T. J. Schmugge, J. R. Wang, and T. J. Jackson, 1982: A model for microwave emission from vegetation-covered fields. J. Geophys. Res., 87, 11229-11237.

NOAA, 1979: Introduction to Weather Radar. U. S. Dept. of Commerce, 70 pp.

Rodgers, E., and H. Siddalingaiah, 1983: The utilization of Nimbus-7 SMMR measurements to delineate rainfall over land. J. Climate Appl. Meteor., 22, 1753-1763.

Savage, R. C., and J. A. Weinman, 1975: Preliminary calculations of the upwelling radiance from rainclouds at 37.0 and 19.35 GHz. Bull. Amer. Meteor. Soc., 56, 1272-1274.

Spencer, R. W., B. B. Hinton, and W. S. Olson, 1983a: Nimbus-7 37 GHz radiances correlated with radar rain rates over the Gulf of Mexico. J. Climate Appl. Meteor., 22, 2095-2099.

_____, W. S. Olson, Wu Rongzhang, D. W. Martin, J. A. Weinman and D. A. Santek, 1983b: Heavy thunderstorms observed over land by the Nimbus-7 Scanning Multichannel Microwave Radiometer. J. Climate Appl. Meteor., 22, 1041-1046.

_____, D. W. Martin, B. B. Hinton and J. A. Weinman, 1983c: Satellite microwave radiances correlated with radar rain rates over land. Nature, 304, 141-143.

Suomi, V. E., R. Fox, S. S. Limaye and W. L. Smith, 1983: McIDAS III: A modern interactive data access and analysis system. J. Climate Appl. Meteor., 22, 766-778.

USDA, 1979: Weekly Weather and Crop Bulletin. U. S. Department of Commerce, 66, No. 29, 23 pp.

Weinman, J. A., and P. J. Guetter, 1977: Determination of rainfall distributions from microwave radiation; measured by the Nimbus-6 ESMR. J. Appl. Meteor., 16, 437-442.

Wilheit, T. T., A. T. C. Chang, M. S. V. Rao, E. B. Rodgers, and J. S. Theon, 1977: A satellite technique for quantitatively mapping rainfall rates over the oceans. J. Appl. Meteor., 16, 551-560.

## Figure Legends

Fig. 1. Composited radar images of all of the rain systems involved in the microwave algorithm development for a) spring, b) summer, and c) fall at 20 km resolution. Image brightness increases linearly with rain rate from 0 mm $h^{-1}$ (dimmest) to 88 mm $h^{-1}$ (brightest).

Fig. 2. Frequency histograms of the rain rates contained in the spring, summer, and fall data sets. The first bar represents the zero rain rate class. Rain rates are after sampling of the data represented in Fig. 1 on a reduced resolution (40 km) grid.

Fig. 3. Images of (a) radar rain rate, (b) V37 $T_B$, (c) V18 $T_B$, and (d) V10.7 $T_B$ at 0610 GMT 21 June 1979 over the eastern United States. The radar rain rates range up to 76 mm $h^{-1}$ while the 37 GHz $T_B$'s range as low as 206 K.

Fig. 4. Average SMMR a) horizontally polarized and b) vertically polarized brightness temperatures for different rain rate classes and different seasons. Each classes average $T_B$'s are represented as a series of connected dots and labeled with the rain rate interval and average rain rate for that class (in mm $h^{-1}$).

Fig. 5. Average values of polarization ($T_B^V - T_B^H$) for the different frequencies and seasons in rain-free areas, illustrating the effects that seasonal variations in soil moisture and vegetative cover have on the observed brightness temperatures.

Fig. 6. Effective emissivities (SMMR $T_B$/surface thermometric temperature) of different surfaces. The corn data were sampled on 9 July 1979 over west-central Iowa. The corn canopy averaged 1.4 m in height. The forest data were sampled at the same time over west-central Arkansas. The Amazon jungle data were sampled from a $1.5 \times 10^4$ $km^2$ area centered at 8°S 56°W in Brazil on 5 July 1979. The mostly unvegetated moist soils were sampled over south-central Iowa on 31 March 1979, while the partly flooded mostly unvegetated soils were sampled over north-central Iowa at the same time. Crop and moisture characteristics were provided by the United States Department of Agriculture (1979).

Fig. 7. The multiple correlation and explained variance achieved at each regression step in the derivation of the spring, summer, and fall equations. The channels chosen by the regression procedure are shown at each step. The dotted line represents the summer equation that results if the analysis is restricted to rain rates less than 20 mm $h^{-1}$. The short line at the bottom shows the correlations achieved if the summer $T_B$'s are compared to 1307 U.S. cooperative network rain gages.

Fig. 8. The explained variance of the radar rain rates as a function of the power to which the GOES-east IR temperatures are raised. Only those temperatures less than 280 K are included in the analysis, resulting in 2040 records from the summer data set.

7/DM6/23

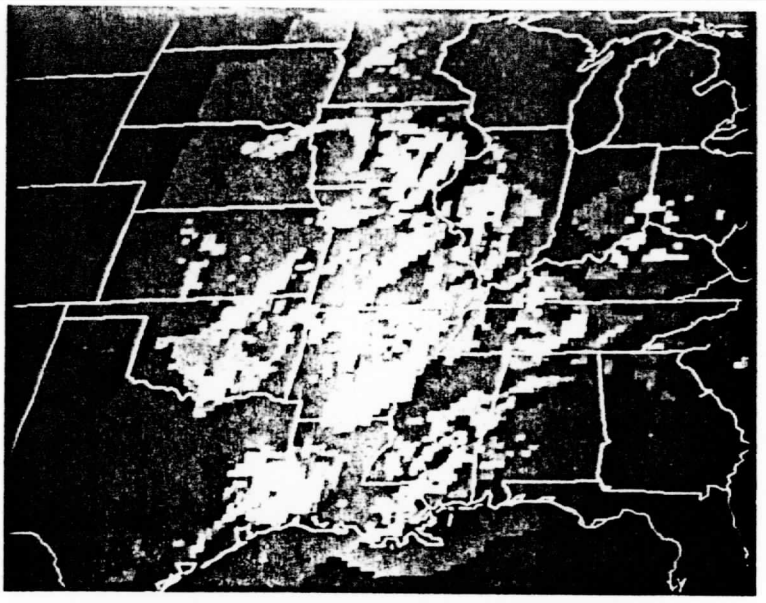

a.

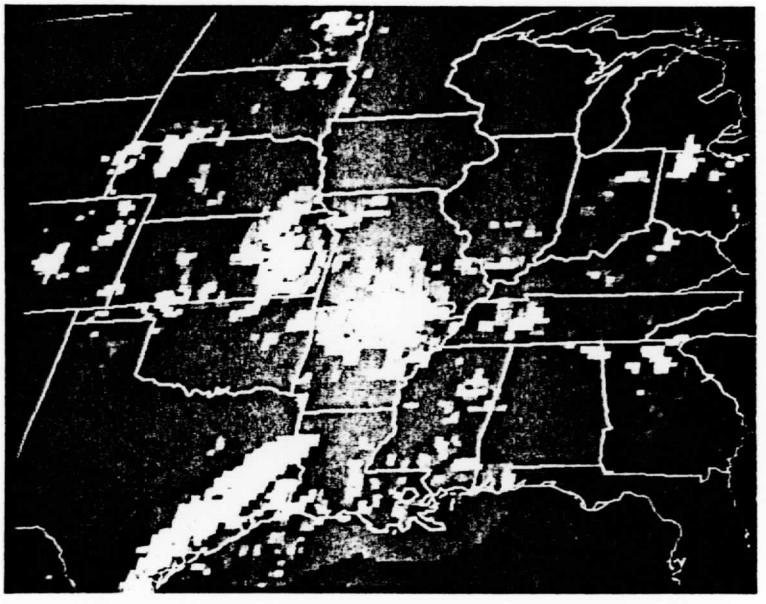

b.

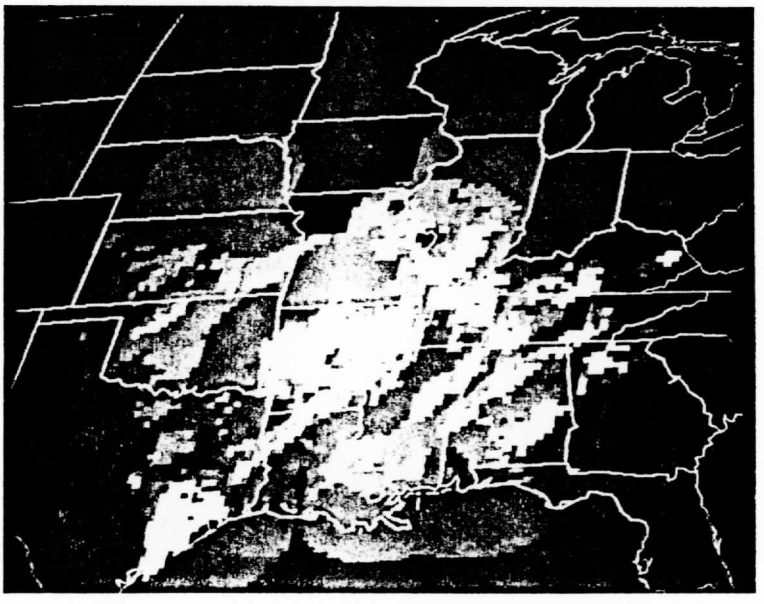

c.

Fig. 1

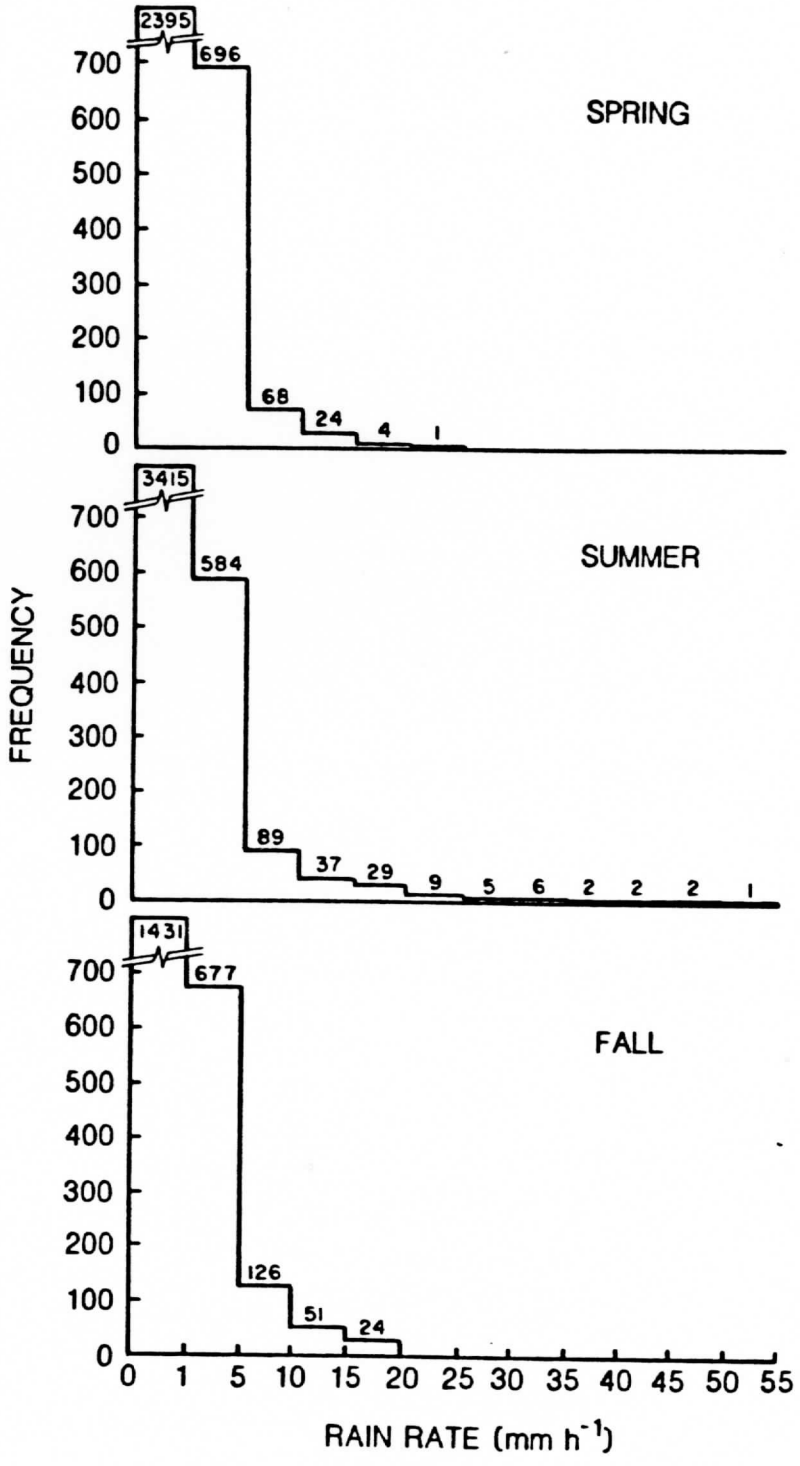
SPRING
SUMMER
FALL
FREQUENCY
RAIN RATE (mm h⁻¹)
2395
696
68
24
4
1
3415
584
89
37
29
9
5
6
2
2
2
1
1431
677
126
51
24
0
100
200
300
400
500
600
700
0 1 5 10 15 20 25 30 35 40 45 50 55

Fig. 2

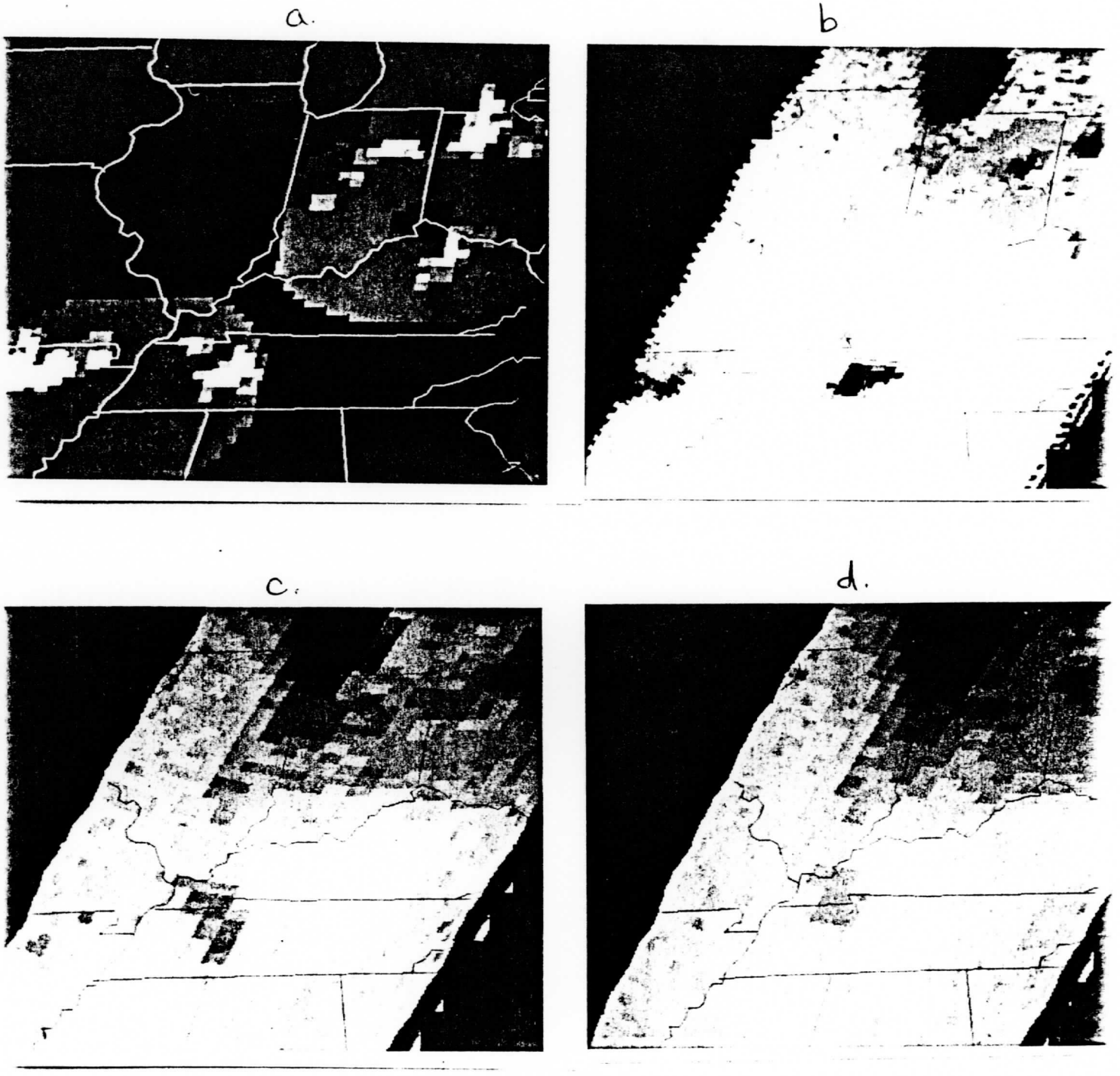


Fig. 3

a.

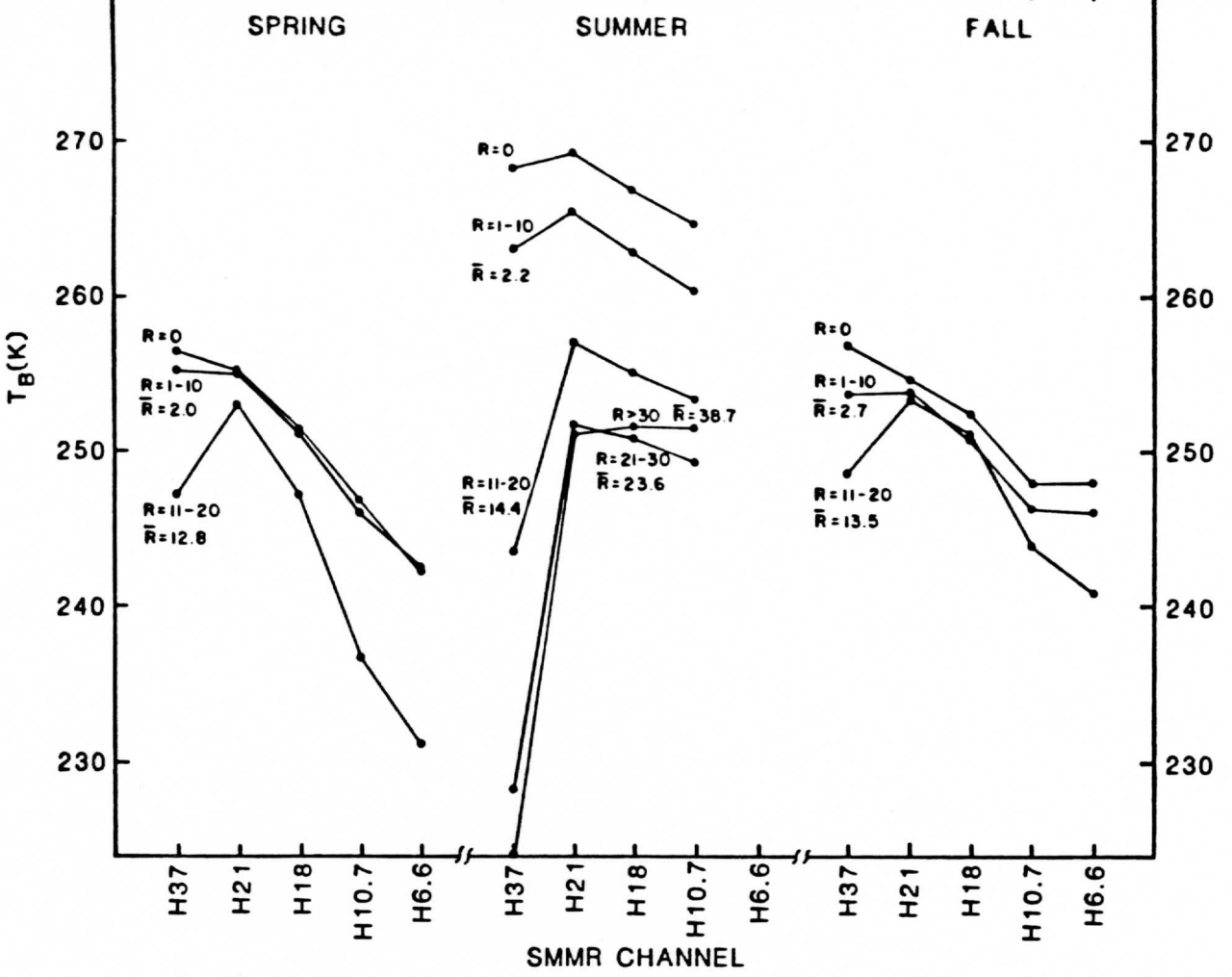
SPRING
SUMMER
FALL
$T_B$(K)
270
260
250
240
230
R=0
R=1-10
$\bar{R}$=2.0
R=11-20
$\bar{R}$=12.8
R=0
R=1-10
$\bar{R}$=2.2
R=11-20
$\bar{R}$=14.4
R>30 $\bar{R}$=38.7
R=21-30
$\bar{R}$=23.6
R=0
R=1-10
$\bar{R}$=2.7
R=11-20
$\bar{R}$=13.5
H37
H21
H18
H10.7
H6.6
SMMR CHANNEL

b.

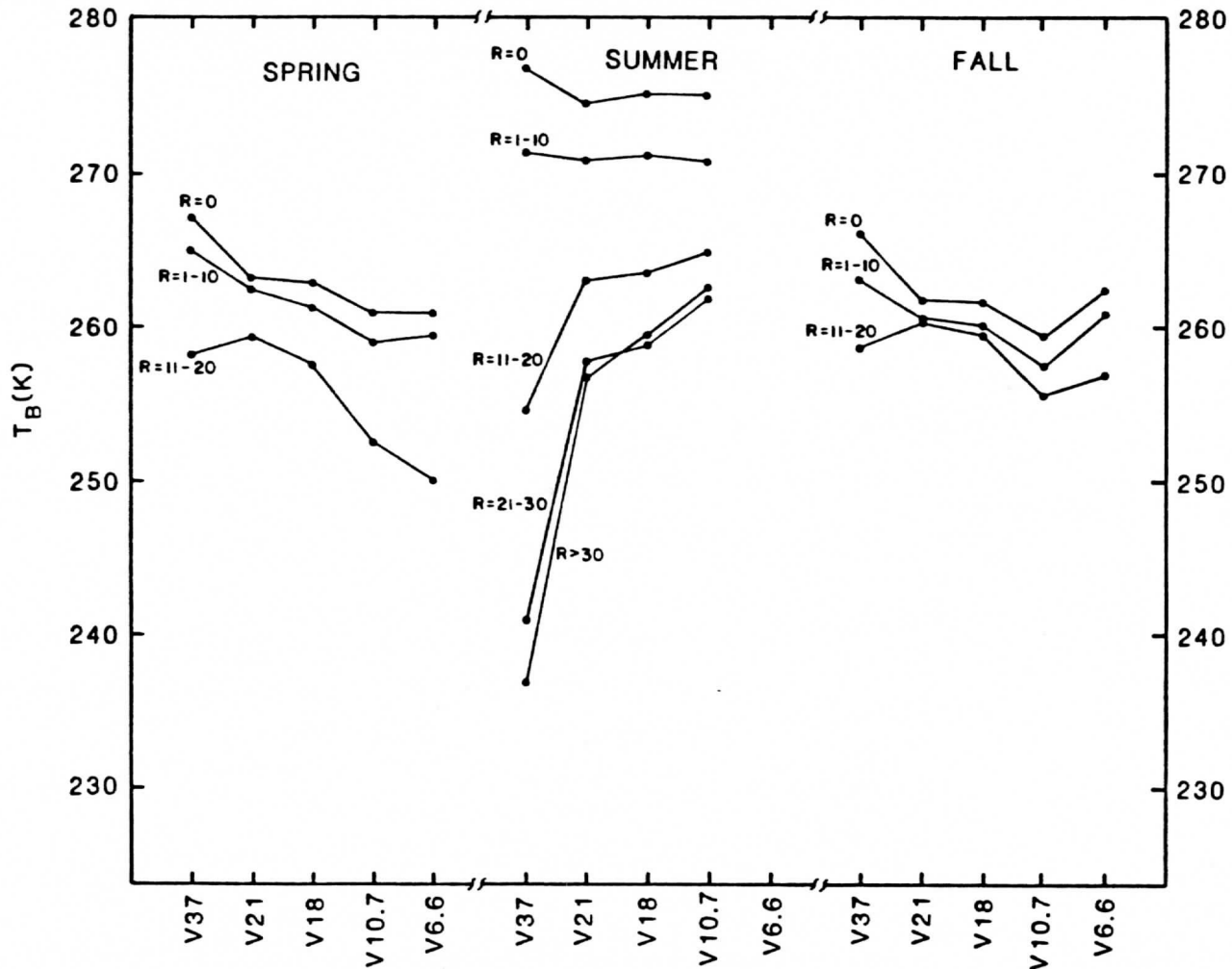
SPRING
SUMMER
FALL
$T_B$(K)
280
270
260
250
240
230
R=0
R=1-10
R=11-20
R=0
R=1-10
R=11-20
R=21-30
R>30
R=0
R=1-10
R=11-20
V37
V21
V18
V10.7
V6.6

Fig. 4

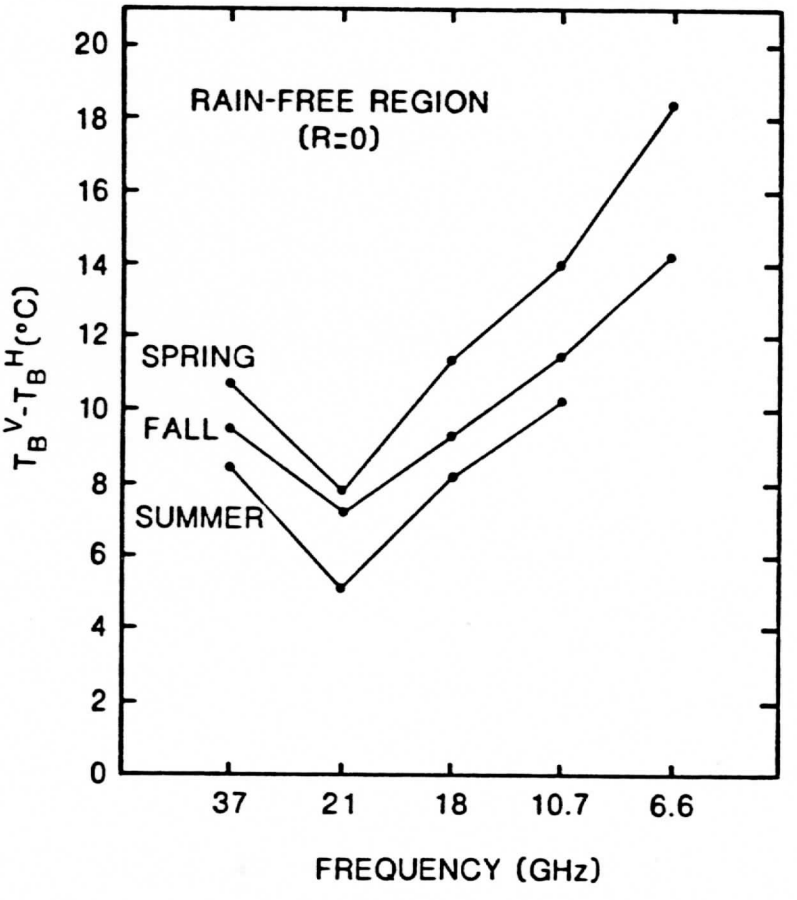
RAIN-FREE REGION
(R=0)
SPRING
FALL
SUMMER
$T_B^V - T_B^H$(°C)
20
18
16
14
12
10
8
6
4
2
0
37
21
18
10.7
6.6
FREQUENCY (GHz)

Fig. 5

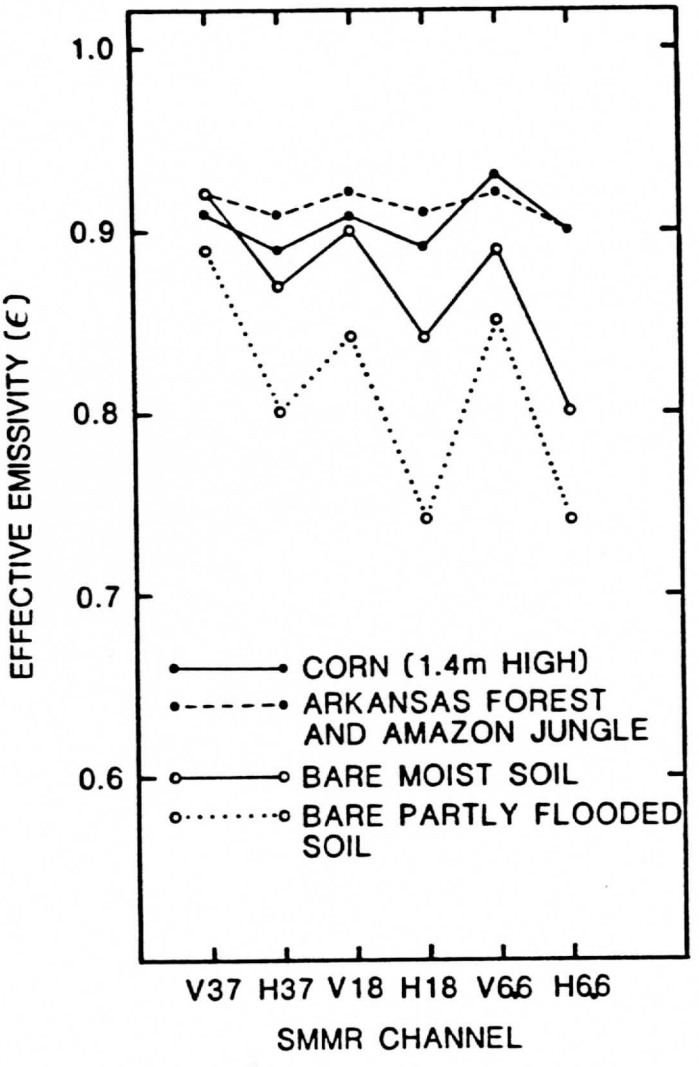
1.0
0.9
0.8
0.7
0.6
EFFECTIVE EMISSIVITY (ϵ)
CORN (1.4m HIGH)
ARKANSAS FOREST AND AMAZON JUNGLE
BARE MOIST SOIL
BARE PARTLY FLOODED SOIL
V37 H37 V18 H18 V6.6 H6.6
SMMR CHANNEL

Fig. 6

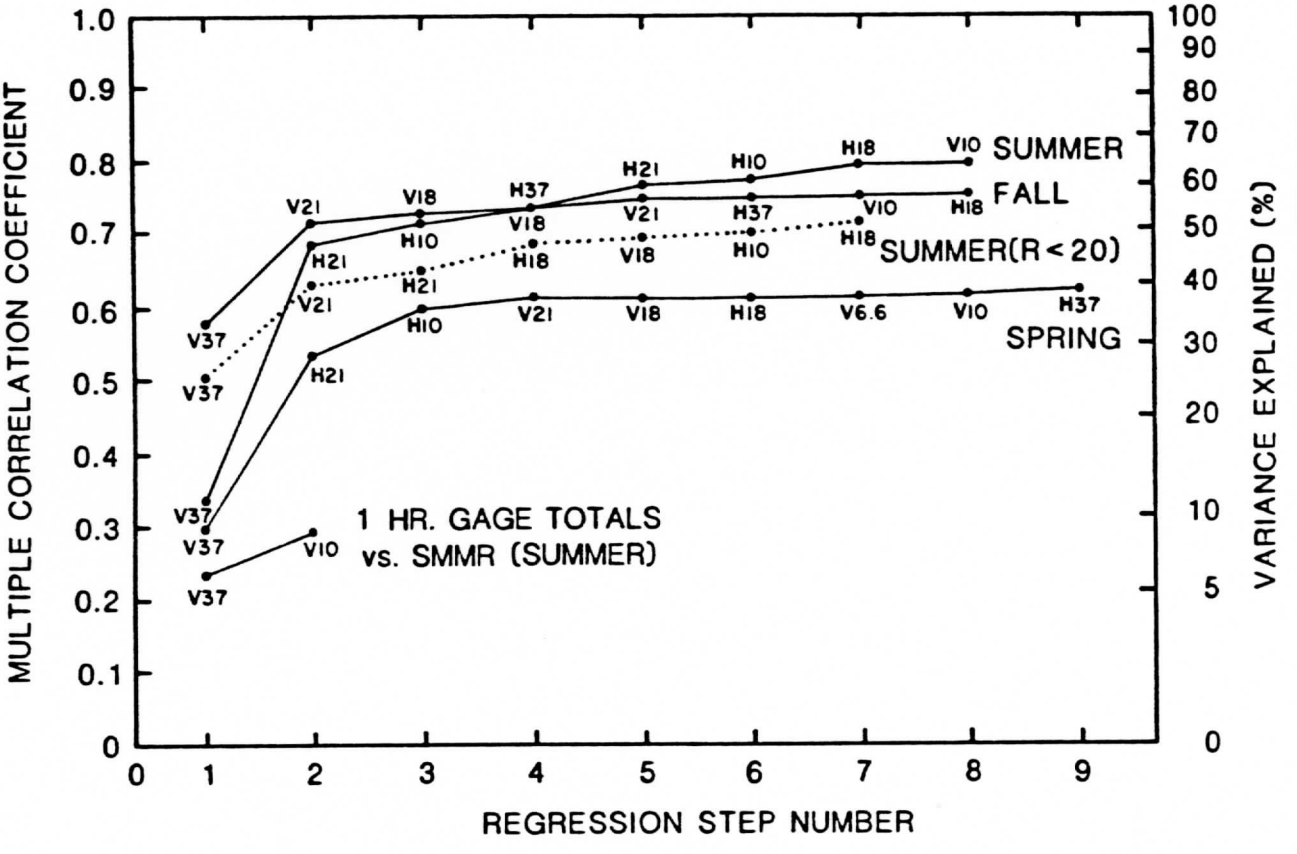
MULTIPLE CORRELATION COEFFICIENT
VARIANCE EXPLAINED (%)
REGRESSION STEP NUMBER
1.0
0.9
0.8
0.7
0.6
0.5
0.4
0.3
0.2
0.1
0
100
90
80
70
60
50
40
30
20
10
5
0
0 1 2 3 4 5 6 7 8 9
V37
V21
V18
H37
H21
H10
H18
V10
SUMMER
FALL
SUMMER(R < 20)
SPRING
V6.6
1 HR. GAGE TOTALS
vs. SMMR (SUMMER)

Fig. 7

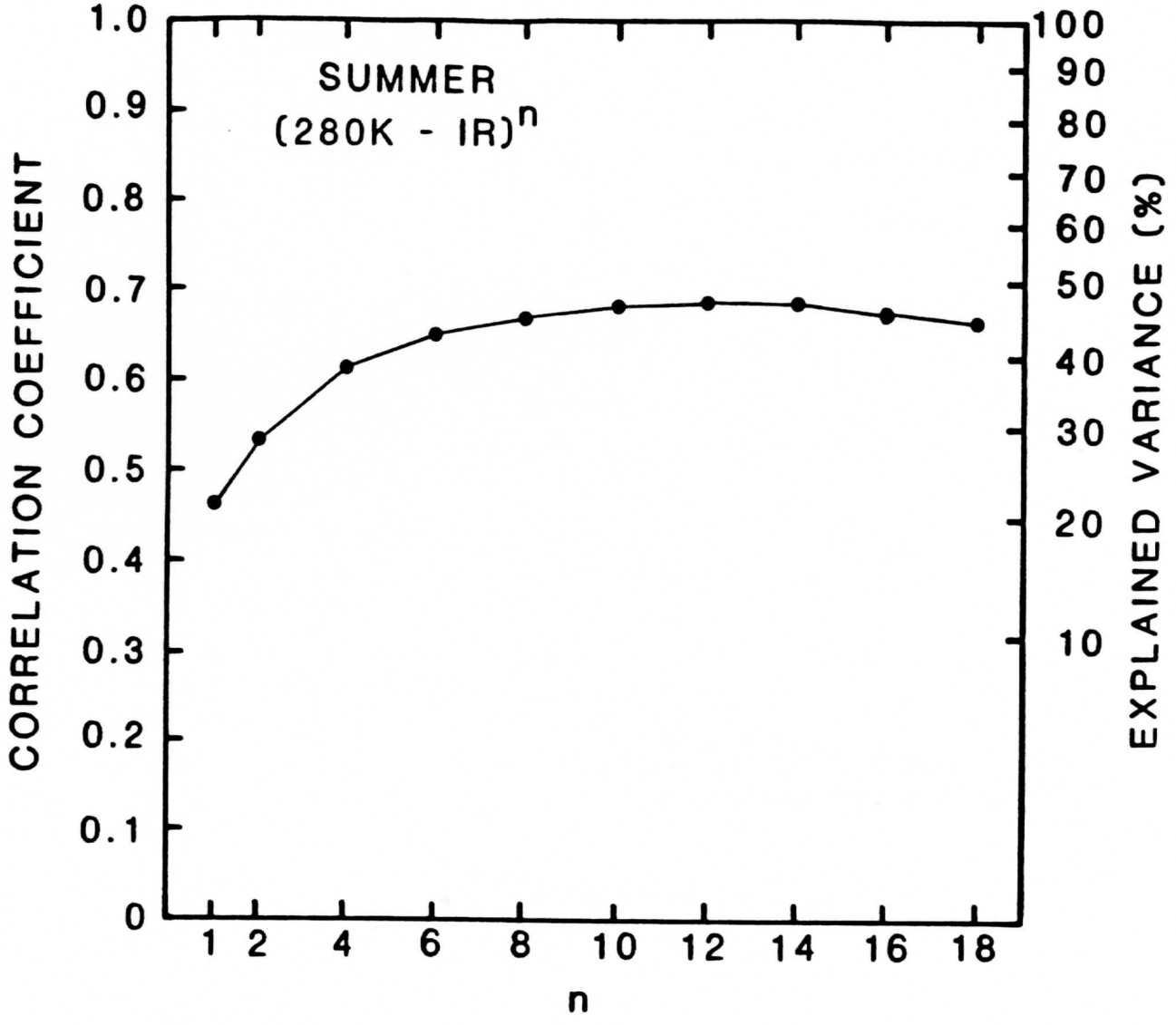
SUMMER
(280K - IR)^n
CORRELATION COEFFICIENT
EXPLAINED VARIANCE (%)
1.0
0.9
0.8
0.7
0.6
0.5
0.4
0.3
0.2
0.1
0
100
90
80
70
60
50
40
30
20
10
1 2 4 6 8 10 12 14 16 18
n

Fig. 8

Appendix 1

# ESTIMATING MONTHLY RAINFALL FROM GEOSTATIONARY SATELLITE IMAGERY OVER AMAZONIA, BRAZIL

by
Elen Maria Camara Cutrim

A dissertation submitted in partial fulfillment
of the requirements for the degree of
Doctor of Philosophy
(Atmospheric Science)
in The University of Michigan
1983

Doctoral Committee:

Professor Fred L. Bartman, Co-chairman
David W. Martin, Co-chairman; Senior Scientist, Space Science Engineering Center, University of Wisconsin
Professor William R. Kuhn
Professor Charles E. Olson, Jr.

ABSTRACT

ESTIMATING MONTHLY RAINFALL FROM GEOSTATIONARY SATELLITE IMAGERY OVER AMAZONIA, BRAZIL

by

Elen Maria Camara Cutrim

Chairmen: Fred L. Bartman, David W. Martin

The infrared regression and the grid-history satellite rainfall estimating techniques were utilized to estimate monthly rainfall in Amazonia during one month of the rainy season (March, 1980) and one month of the dry season (September, 1980). The estimates were based on 3-hourly SMS-II infrared and visible images.

Three sets of coefficients for the grid history method (Marajo, Arabian Sea, and GATE) were used to estimate rainfall. The estimated rain was compared with gauge measurements over the region. The infrared regression technique overestimated by a factor of 1.5. The Marajo coefficients yielded the best estimate, especially for eastern Amazonia. In the wet month Marajo coefficients overestimated rain by 10% and in the dry month by 70%. The Arabian Sea coefficients overestimated rain and the GATE coefficients slightly underestimated rain for Amazonia.

Two maps of monthly rainfall over Amazonia were constructed for March and September, 1980, combining the ground station and satellite inferred rainfall of the grid history method using the Marajo coefficients. The satellite observations and ground data were mutually compatible and were contourable on these final, composite maps. Monthly rainfall was found to be much more inhomogeneous than previously reported. In March there was a belt of high

precipitation trending southwest, with higher values and sharpest gradients in the coastal area. The upper Amazon was also an area of high precipitation, both north and south of the equator. In Roraima rainfall decreased drastically to the north. In September, the area of highest precipitation was the northwestern part of Amazonas State (northern hemisphere). Rainfall elsewhere was very localized and in northeastern Amazonia varied from 0 to 150 mm. Even though the grid history method presented better results for estimating rainfall over Amazonia, the IR model could be utilized more efficiently and economically on an operational basis if the calibration were properly made with longer sampling period and better distribution of ground observations.

Appendix II

# AUTOMATED CLASSIFICATION OF RAINFALL RATES

# USING STATISTICAL PATTERN RECOGNITION

Bonita G. Lee and Roland T. Chin*
Department of Electrical and Computer Engineering
University of Wisconsin-Madison

David W. Martin
Space Science and Engineering Center
University of Wisconsin-Madison

## Abstract

This paper describes an automatic rainfall rate classification procedure which uses statistical pattern recognition techniques. The procedure, using spectral and textural features extracted from visible and infrared satellite images, was applied to classify 8 km × 8 km windows of GOES imagery into one of three classes: no, light, and heavy rain. The training process utilizes both weather radar and cloud development information derived from image sequences. Images from three different days were tested and classification accuracies of 70% and better were obtained. An automated scheme of this type has the potential to relieve the rainfall rate estimation process from tedious manual interpretation while achieving comparable accuracy.

Keywords - Statistical pattern recognition, Automatic rainfall rate assignment, Remote sensing data, Classification, Feature Extraction.

---

*Address all correspondence to Roland T. Chin.

This work was supported in part by the Engineering Experiment Station, the Space Science and Engineering center under NOAA contract NA-81-AAH-00024, and the Department of Meteorology.

Appendix III

# GRID HISTORY: A GEOSTATIONARY SATELLITE TECHNIQUE FOR ESTIMATING DAILY RAINFALL IN THE TROPICS

By

David W. Martin

Michael R. Howland

Space Science and Engineering Center
University of Wisconsin-Madison
Madison, WI 53706

Submitted to

Journal of Climate and Applied Meteorology

May 1984

Abstract

We describe a new technique for estimating daily rainfall by means of visible and infrared geostationary satellite imagery. The technique is designed for the tropics and warm-season mid-latitudes. Because it operates on a grid of points and measures time changes at these points the technique has been named grid history.

It is assumed that at any grid point of an image in a sequence, by means of spectral, textural and evolutionary information, it is possible to classify instantantaneous rain rate as either nil, light, moderate or heavy. Then the total rainfall over a day is the sum of the frequencies of each class times the class average rate.

The class average rates have been determined by least squares multivariate linear regression of frequencies on observed rainfalls. The areas treated are South China Sea, India, Arabian Sea, tropical North Atlantic Ocean and Amazonia. Inland India had the lowest (driest) class average rates (coefficients), coastal India the largest (wettest) coefficients. Differences in coefficients were least for the Arabian Sea and Atlantic Ocean. There the class average rates were roughly 0 (by definition), 1.5, 6 and 15 mm $h^{-1}$. For the strongly convective rain regimes here treated, it was found to be important to "look" at the area at least once per hour. A loss of accuracy in estimates over land apparently was due to unexpectedly large terrain and synoptic effects. Best-circumstance estimates of daily rainfall for an area 100 km on a side should be within a factor of two of true rainfall.